Energy Technology
Generation, Conversion, Storage, Distribution
www.entechnol.de

Air-Cathode with 3D Multiphase Electrocatalyst Interface Design for High-Efficiency and Durable Rechargeable Zinc–Air Batteries

Sadegh Askari, Davide Mariotti, Ruairi McGlynn, and Jan Benedikt*

The development of rechargeable zinc–air batteries is hindered by the low energy-conversion efficiency and the short cycle life, which are partly due to the unsatisfactory performance of the oxygen electrocatalysts on the air-cathode. The low performance of the catalysts is partially due to the complexity of the gas-involving multiphase interface required for the oxygen catalysis reactions, and it is often acquired only for a fraction of the loaded catalyst that is in direct contact with the 2D surface of the gas diffusion layer (GDL). A paradigm is proposed for extending the active region using an enhanced 3D multiphase interface on the cathode, which comprises abundant active sites with optimized hydrophobicity and reliable stability. The oxygen reduction reaction (ORR) or the bifunctional catalyst is embedded into the bulk of the GDL and forms a semihydrophobic catalyst layer (SCL), whereas an auxiliary hydrophilic oxygen evolution reaction (OER) catalyst layer integrated onto the GDL assists to reduce the polarization during the cell charging and improves the cathode durability. An air-cathode comprising the SCL exhibits an overall performance superior to the conventional cathode counterparts including cathodes with metal-based catalysts, due to the enhanced and optimized multiphase interface on the cathode.

High-performance electrochemical energy conversion and storage devices such as metal–air batteries, fuel cells, and water-splitting cells play a fundamental and essential role in the development of green and sustainable energy technologies. The performance of these renewable technologies relies on the efficiency of the electrochemical reactions at the device electrodes, including oxygen evolution reaction (OER) and oxygen reduction reaction (ORR). At the air-cathode of metal–air batteries and in particular for zinc–air batteries, these oxygen electrocatalytic reactions are crucially important and determine the overall performance of the device. Indeed, the significant theoretical energy density of 1086 Wh kg^{-1}—around five times higher than the present lithium-ion batteries—durability, and satisfactory energy efficiency of the zinc–air batteries remain unattainable without efficient oxygen catalysis.[1–3] Unfortunately, the state-of-the-art noble metal Pt and Ir/Ru-based catalysts for ORR and OER suffer from drawbacks such as scarcity, poor durability, and negative environmental impacts and thus have to be replaced with novel catalysts. Therefore, extensive effort has been devoted to finding efficient nonprecious catalysts including non-noble transition metals and carbon-rich catalysts.[2,4–12] Various bifunctional catalysts with outstanding performances in zinc–air batteries have been reported within the last years.[13–19] Despite the significant progress, the performance of the catalysts integrated into the air-cathode of two-electrode battery devices still remains far from satisfactory. The low performance is partially due to the substantially large overpotential induced by the absorption-energy scaling relations of the reaction intermediates (*OOH, *OH) involved in the oxygen electrocatalysis and the efforts to circumvent that has not been successful especially on bifunctional catalysts.[20,21]

In addition to the intrinsic catalyst activity of bifunctional catalysts, the design of the catalyst interface is equally important on a bifunctional air-cathode assembly though it has received less attention in previous studies.[22–24] The electrochemical reactions on the electrode occur at the complex multiphase interface of the gaseous reactant/products, liquid electrolyte, and the solid catalysts, where the electrons and reactants have access to the active sites. In particular, ORR requires a semihydrophobic environment with optimized access of the catalyst to the oxygen and the aqueous electrolyte, whereas OER occurs in the liquid electrolyte and solid catalyst interface and is more compatible with a hydrophilic environment. An ideal cathode architecture would provide a large amount of stable and active sites at the optimized multiple-phase interface, whereas the charge and reactant transfer resistances maintain low. The fulfillment of these conditions

Dr. S. Askari, Prof. J. Benedikt
Institute of Experimental and Applied Physics
Kiel University
Leibnizstraße 17, 24118 Kiel, Germany
E-mail: askari@physik.uni-kiel.de

Prof. D. Mariotti, Dr. R. McGlynn
Engineering Research Institute (ERI)
Ulster University
Northern Ireland BT37 0QB, UK

The ORCID identification number(s) for the author(s) of this article can be found under https://doi.org/10.1002/ente.202000999.

DOI: 10.1002/ente.202000999

is hardly acquired on a conventional air cathode that is typically fabricated by loading (e.g., drop-casting or pressing) the hydrophilic bifunctional catalyst layer onto the hydrophobic gas diffusion layer (GDL). It is frequently observed that the catalyst layer cannot withstand the harsh oxidizing and caustic environment on the bifunctional air cathode of rechargeable zinc–air batteries due to the degradation of the binder (catalyst detachment) or agglomeration of the active catalyst.[3] Moreover, the multiphase interface is limited to a nearly 2D layer on the flat GDL surface, and only a fraction of the catalyst locates in this active region.

Notably, the low solubility and slow diffusion rate of the oxygen in aqueous electrolytes restricts the ORR efficiency of the catalyst. For instance, in 6 M KOH, the concentration of dissolved oxygen is reduced to 78.1 μM. An approach to increase the accessibility of the oxygen is the chemical surface modification of the catalyst. For instance, surface passivation of carbon-based catalysts with oxygenophilic ionic-liquid enhances the ORR activity.[25,26] Another challenging issue is the transport of the oxygen bubbles on the gas-generating OER catalyst surface; it is, however, alleviated on hydrophilic and uneven catalyst surfaces comprising micro/nanostructures. The bubble adhesive force is reduced by improving the superaerophobic properties of the nanostructured electrodes in favor of the OER.[23,27,28]

To address the issues involved with the conventional 2D reactive interface, we propose a cathode structure with enhanced and optimized interfacial catalytic reactions. The principle idea is to integrate layers of active materials that provide enlarged 3D reactive regions optimized for ORR and OER and benefits from abundant active sites, facilitated diffusion pathways, high electric conductivity, and mechanical stability. A practical approach is to build a GDL with the active layers embedded into its bulk. Therefore, the catalyst covers the porous GDL on the electrolyte facing side toward the interior bulk and acquires a certain thickness, whereas the rest of the GDL remains intact. Ideally, the catalyst has to firmly adhere to the conductive carbon surface inside GDL and balance the hydrophobicity in the presence of the hydrophobic polytetrafluoroethylene (PTFE) binder.

The commercially available carbon-based GDL typically consists of a fully hydrophobic macroporous backing layer (graphitized carbon fibers) that is covered with a microporous layer with fine porosity for loading catalysts and composed of mixture of carbon black and PTFE. To examine the idea of the 3D multiphase interface, we passivate the surface of porous carbon in the GDL microporous layer by oxygen carboxyl and carbonyl functional groups. These functional groups provide ORR/OER active centers on the carbon surface and enhance the hydrophilicity of the layer. The functionalized region of the GDL forms a semihydrophobic catalyst layer (SCL) on the electrolyte-facing side, in which the amount of active centers and the hydrophobicity is tunable. Schematics of a conventional air-cathode and the cathode with the SCL are shown in **Figure 1**a,b, respectively. The GDL with the active SCL operates as a self-standing bifunctional cathode and hereafter is referred to as SCL-C.

The performance of the SCL-C is further improved by adding a hydrophilic permeable layer of the active OER layer on the GDL (Figure 1c). Adding this OER active layer reduces the charge voltage of the cell and protects the SCL against severe oxidative conditions, which is critically important for improving the efficiency and life-time of the cell at higher charge/discharge currents. Separating the OER and ORR active regions is generally advantageous due to the easier optimization and manipulation of the monofunctional catalysts, which are more flexible in terms of their intrinsic activity and morphology design.

For preparation of the SCL-C (Figure 1b), two different approaches were used to passivate the carbon surface with the oxygen functional groups. The first method was a gas-phase

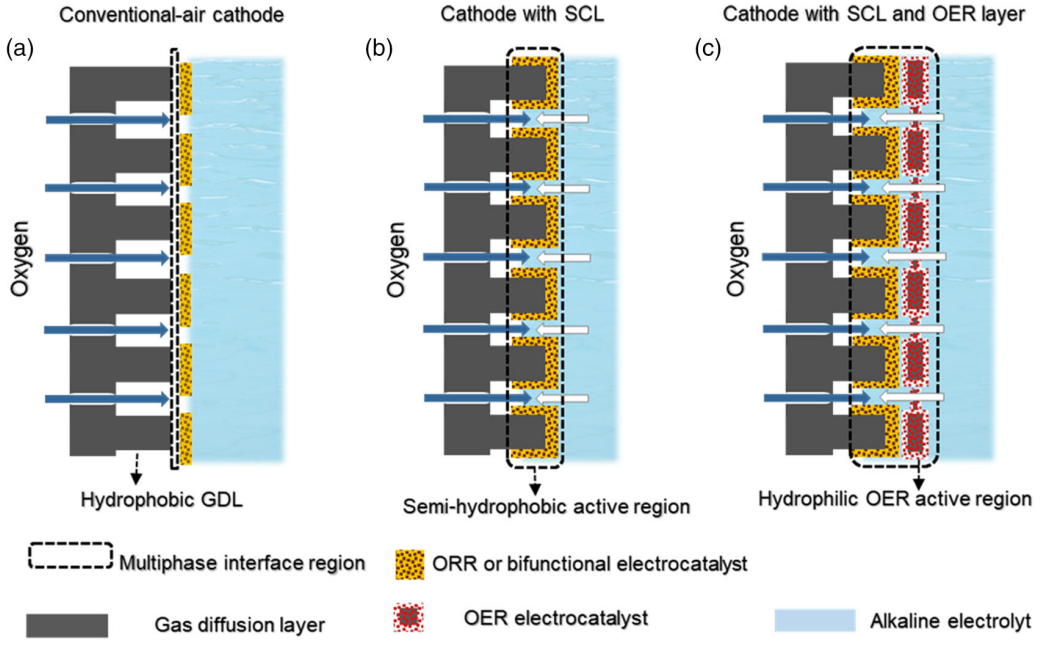

Figure 1. The concept of an air cathode with an enhanced 3D multiphase catalyst interface. a) Conventional air cathode, b) air cathode with the SCL-C, and c) air cathode with the SCL and an auxiliary OER layer.

method, in which the electrolyte-facing side of the GDL is exposed to a low-pressure argon/oxygen radiofrequency plasma for several minutes. The second method is based on a sustainable chemical treatment approach using nitric acid passivation at low temperature (see Experimental Section for more details). The electrochemical measurements reveal that both these methods significantly promote the ORR/OER activity, though the overall ORR/OER performance of the chemically treated carbon paper is superior. Plasma treatment severely etches the carbon surface and creates a rough surface with abundant edges and 2D structures (Figure S2, Supporting Information). In contrast, the surface morphology of the carbon fibers exposed to the chemical treatment, shown in Figure S1, Supporting Information, remains unchanged at least in the limit of the scanning electron microscopy (SEM) resolution. In addition to that, the hydrophobic surface of the GDL paper is rapidly changed to a highly hydrophilic surface upon the plasma exposure, so that the water droplets rapidly permeated the treated GDL. This may explain the lower ORR catalytic performance of the plasma-treated carbon paper. Hereafter, we focus on the results of the chemically treated GDL due to its higher performance, and the flexibility of the method in terms of the control over amount of catalytic active sites and hydrophilicity. The effectiveness of the SCL-C is evaluated by comparing the performance of this configuration with the performance of the conventional cathode (Figure 1a). The latter one is prepared using powdery carbon black treated in a similar treatment process. The SCL-C performance is also compared with the conventional cathode comprising precious metal-based catalysts, and with the previous reports using various catalysts.

X-ray photoelectron spectroscopy (XPS) results confirm that the oxygen content of the GDL and carbon black is increased after chemical surface treatment. The survey spectra of the pristine GDL and the SCL-C representing the presence of carbon, oxygen, and fluorine bonds are shown in **Figure 2**a. Similar spectrum with lower percentage of fluorine is obtained for the chemically treated carbon black loaded on the GDL (named Con-C), shown in Figure S4, Supporting Information. The additional fluorine peaks observed in the survey spectra are due to the PTFE binder in the GDL. For the carbon paper, the overall oxygen content is increased from 3.6% in pristine GDL to 7.1% in chemically treated SCL-C. Further analysis of the high-resolution carbon and oxygen bonds indicates the presence of different oxygen-containing functional groups on SCL-C. Figure 2b shows the carbon 1*s* profile deconvoluted to several peaks. The peaks at 284.5 eV represents the graphitic carbon and the peak 285.1 eV is attributed to the carbon defects.[29] The peaks at higher binding energies originate from the carbon oxygen bonds: C—O (286.0 eV), C═O (287.5 eV), and O—C═O (288.9 eV). The band around 291.5 eV is deconvoluted into two components at 291.25 and 292.0 eV that correspond to the π–π^* transitions and the C—F_x bonds.[29] The high-resolution O 1*s* peak (Figure 2c) can be deconvoluted into two components: double bound (C═O) at 531.6 eV and single bound (C—O) at 533.1 eV.[29] Notably, the amount of carboxyl or ester (COOH) type groups is considerably increased after treatment, which agrees very well with previous reports on carbon treated by nitric acid.[30]Moreover, the surface wettability of the GDL is enhanced upon surface passivation with oxygen functional groups. The contact angle is decreased from 133° on GDL to 74° on SCL-C (Figure 2d), indicating that the GDL surface is converted to a semihydrophobic surface after treatment. It is noteworthy that the back side of the GDL remains intact upon chemical treatment, which has been confirmed by the contact-angle measurements on both sides of the treated GDL (Figure S5, Supporting Information). Figure 2e shows several different oxygen groups and the developed defect sites typically observed on oxidized carbon. Upon oxidation, various oxygen-functional groups graft the carbon surface including carboxyl, hydroxyl, carbonyl, ether, quinone, and anhydride

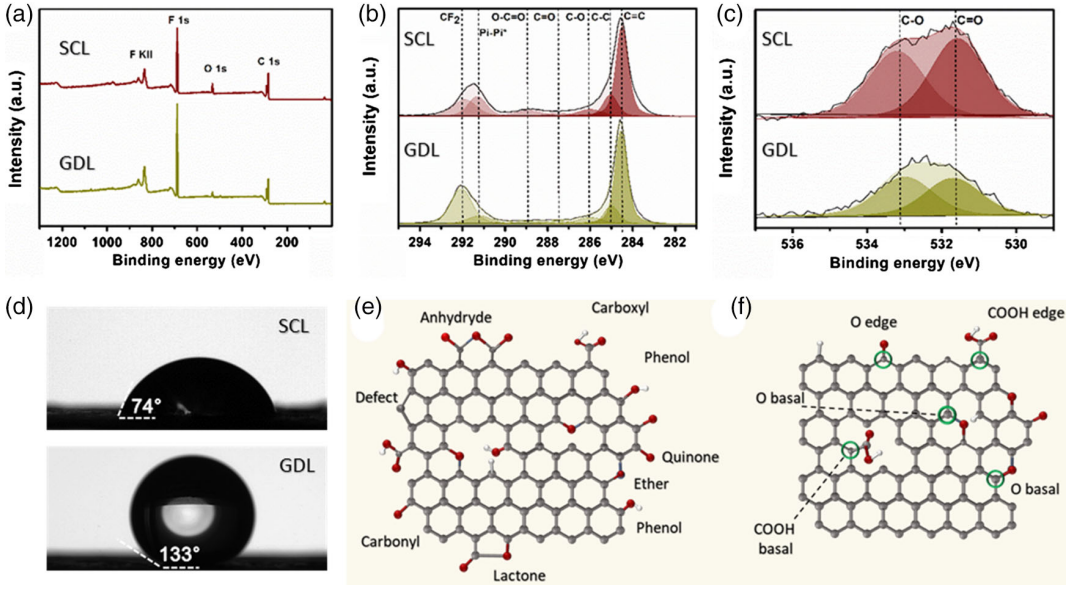

Figure 2. a) XPS survey spectra and high-resolution XPS spectra of the b) C 1*s* and c) O 1*s* bands for GDL and SCL-C, d) contact angle on the SCL-C and GDL, e) illustration of the different oxygen-containing surface groups on carbon, and f) schematic of functional oxygen groups on carbon atoms with the highest activity toward ORR and OER derived from DFT calculations. The carbon atoms denoted with a green circle are the active sites.

groups. The ratio of the different oxide groups alters depending on the oxidation method and the treatment temperature; i.e., although liquid-phase oxidation in nitric acid at low temperature lead to the dominant formation of carboxylic groups, gas-phase oxidation increases the carbonyl/quinone, anhydride, lactone, phenol groups.[30]

It is known that specific oxygen functional groups can mediate ORR on carbons. The ORR activity is specifically further pronounced on activated carbon in high pH solutions. For instance, initial studies revealed that the quinone-type functional groups on carbon electrodes (e.g., glassy carbon) enhances the O_2 reduction current in alkaline solutions.[31,32] The adsorbed oxygen groups redistribute the electric charge on the carbon atoms due to the higher electronegativity of the oxygen. Notably, the adsorption of the intermediate species of the OER and ORR is enhanced on positively charged carbon atoms and it could significantly enhance the OER and ORR performance depending on the structure of the oxygen functional group. Numerical models based on density functional theory (DFT) calculations predict that some of the oxygen group configurations provide highly active sites toward ORR or OER with the activity remarkably comparable to the benchmark precious metal based catalysts.[33,34] Figure 2f shows the sites with highest activity toward ORR and OER on oxidized carbon surface predicted by DFT calculations. Among the studied oxygen groups, the carboxyl and carbonyl groups provide very low overpotentials for both ORR and OER comparable to the values reported for the Pt and Ru-based catalysts, respectively, while for instance the hydroxyl groups located at the edge or in basal plane provide a lower activity.[33,34]

The oxygen electrocatalytic performance of the samples was evaluated in 1.0 M KOH using a three-electrodes electrochemical cell and compared with control samples. The ORR activity was first measured by cyclic voltammetry (CV) in N_2 and O_2 saturated electrolytes. The CV curves in **Figure 3**a were collected within the ORR potential window at scan rate of 20 mV s^{-1}. The GDL displays a relatively low background capacitance that is comparable to the Con-C and Pt/C + RuO_2 samples. After surface treatment, the double-layer capacitance of the SCL-C is drastically increased indicating the larger surface area accessible to the electrolyte. This was further evaluated by measuring the double-layer capacitance in a nonfaradaic potential window (Figure 3b and Figure S6, Supporting Information). The polar oxygen-containing groups on the carbon surface enhance the hydrophilicity and thus the accessible surface area to the aqueous electrolyte on the SCL-C. Apart from the background current, all the electrodes show a reduction peak in O_2 saturated electrolyte (Figure 3a). The CV profile of the SCL-C electrode displays an onset potential around 0.90 V and a distinct cathodic reduction peak at 0.79 V. The peak current density is effectively increased relative to the pristine GDL with a weaker peak at 0.72 V. Similar reduction peak is observed on the Con-C with peak position at 0.78 V and an onset around 0.88 V. The positive shift of the reduction peak on carbon electrodes after passivation with oxygen groups has been previously observed.[35] The CV peak in 1.0 M KOH on glassy carbon treated with oxygen groups was at –0.234 V (vs Ag/AgCl) in the report of Xu et al.[35] which is comparable to the peak position observed for the CV of our SCL-C and Con-C electrodes. The positive shift in the onset potential to higher than 0.85 V and the increase in the peak current demonstrates a significant enhancement of ORR activity on oxidized carbon electrodes.

To further study the ORR performance, the linear sweep voltammetry (LSV) measurement was carried out on a rotating disk

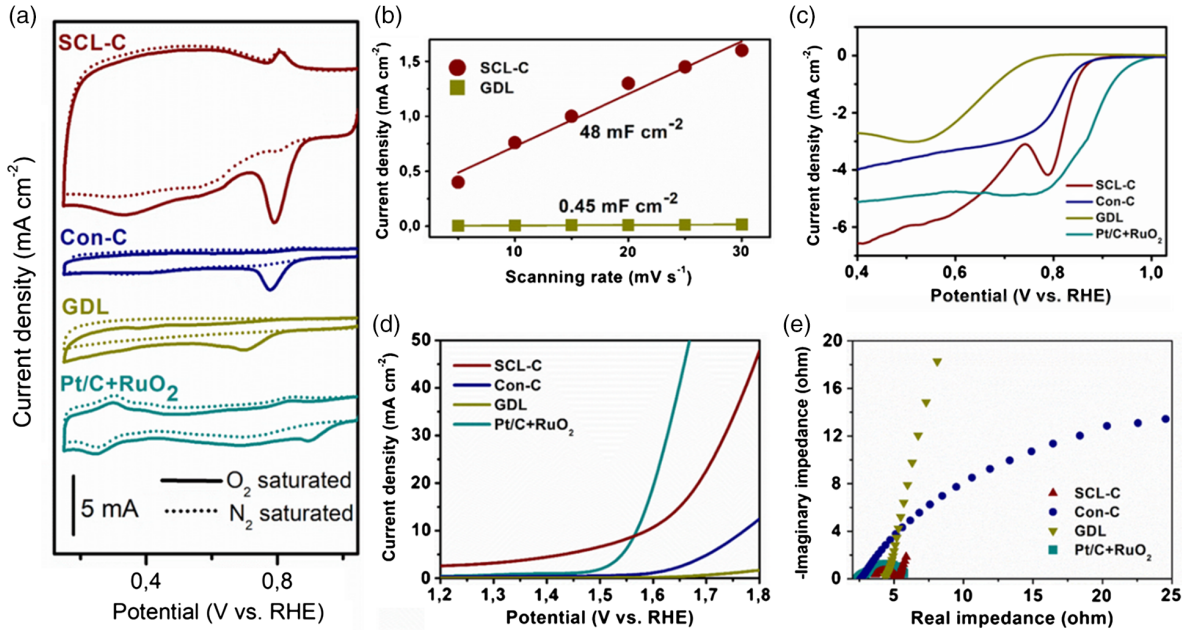

Figure 3. a) CV curves showing ORR activity for different electrodes in O_2 and N_2 saturated 1 M KOH at a scanning rate of 20 mV s^{-1}, b) electrochemical evaluation of the double-layer capacitance for the SCL-C and pristine GDL, c) polarization curves within the ORR potential window at a scanning rate 5 mV s^{-1} and a rotation speed of 1600 rpm, d) polarization curves within the OER potential window at a scanning rate of 5 mV s^{-1}, and e) Nyquist impedance spectra of the electrodes at potential of 0.6 V (vs Ag/AgCl).

electrode. The LSV curves shown in Figure 3c are corrected by subtracting the double-layer current. The typical shape of the LSV profile (Figure 3c) with a prewave at lower overpotentials that is frequently reported on carbon electrodes is observed and it is more pronounced on the SCL-C.[36] An earlier current drop or a positive shift in the onset potential accompanied with a larger steady current represent a higher ORR performance. On the SCL-C, the onset potential has a distinct positive shift relative to the GDL electrode. Furthermore, a clear reduction prewave is observed at potential of 0.79 V and it is followed by a second reduction wave starting at around 0.74 V. The current density values of the SCL-C is apparently higher than the pristine GDL and Con-C and is comparable to the noble metal electrode, indicating a very good catalytic activity toward ORR. That is compatible with the CV profiles in Figure 3a and the higher active surface area measured on SCL-C. Studies of similar carbon materials such as carbon black, carbon nanotube, and microfibers passivated with oxygen functional groups reveal that oxygen reduction undergoes a dominant two-electron pathway in alkaline solutions.[31,34,35,37,38] Notably, the two-wave shape of the profile collected for ORR (Figure 3c) is probably due to the occurrence of a two-step reduction reaction, as it has been reported previously.[37] The first step is reduction of the oxygen molecules to hydrogen peroxide, which has been widely observed on carbon materials. The second step is the partial reduction of the produced hydrogen peroxide at larger overpotentials. Therefore, the total number of electrons could be higher than 2, as it has been observed on similar carbon materials.[37]

Figure 3d shows the OER polarization curves collected in 1.0 M KOH. The OER activity of the GDL sample is very poor so that the current density is limited to lower than 1 mA cm^{-2} at overpotential 539 mV. The OER current is partially increased after loading treated carbon black on the GDL (the sample Con-C). However, the OER performance of the GDL is remarkably enhanced upon surface treatment (SCL-C sample). In particular, the overpotential acquired at current density of 10 mA cm^{-2} on the SCL-C is 362 mV that is only slightly higher (≈24 mV) than the value recorded for the $Pt/C + RuO_2$ electrode. The electrochemical impedance measurement performed at 0.6 V (vs Ag/AgCl) shows that the SCL-C has a charge-transfer impedance comparable to $Pt/C + RuO_2$ electrode (Figure 3e).

The overall three-electrode analysis shows that the surface treatment effectively improves the ORR/OER catalytic activity of the SCL-C and Con-C samples. Adding SCL layer based on oxygen functional groups practically converts the GDL into a bifunctional ORR/OER active electrode with a performance approaching the noble metal-based electrode. The measurements show that the accessible surface area to the aqueous electrolyte on carbon paper significantly increases after surface treatment that is explained by the enhanced hydrophilicity of the passivated carbon surface. The microporous structure provided in the carbon-based 3D SCL layer facilitates the mass transport of the electrolyte and the access to the vast number of active sites that benefits from a modified multiphase interface in a regulated semihydrophobic environment.

The results from the electrochemical measurements indicate that adding 3D SCL significantly boosts the ORR and OER activity of GDL, so that the overpotentials on the SCL-C approach those of the $Pt/C + RuO_2$ catalyst. In light of that, the performance of the SCL-C and Con-C are evaluated in a zinc–air battery assembly as an example of a practical energy-storage device. These electrodes are directly used as a self-standing air-cathode of the battery and a Zn foil serves as an anode in 6 M KOH (**Figure 4**a). The performance of the powdery $Pt/C + RuO_2$ is also evaluated by loading it onto a pristine GDL.

The battery made with the SCL-C electrode presents a high open-circuit voltage of 1.42 V which is slightly lower than the value 1.45 V measured for the $Pt/C + RuO_2$ electrode. Figure 4b shows the discharge profiles for the as-fabricated cells. It can be seen that the $Pt/C + RuO_2$ electrode shows a lower overpotential relative to other electrodes. The higher discharge voltage of the $Pt/C + RuO_2$ electrode is in accordance with the ORR three-electrode analysis of the catalysts. The charge voltage is notably decreased on carbon electrodes after surface treatment (see Figure 4c and Figure S7, Supporting Information). At the voltage of 1.0 V, the SCL-C exhibits a current density of 92 mA cm^{-2} that is close to the value obtained for the Con-C (loading 0.8 mg cm^{-2}). At lower current densities (<20 mA cm^{-2}), discharge (charge) voltage of the SCL-C is higher (lower) than the Con-C. The power density diagrams of the batteries are shown in Figure 4b. The peak power density of the SCL-C and Con-C exceeds the value of 150 mW cm^{-2}.

Although the cell with the $Pt/C + RuO_2$ catalyst operates with a low charge–discharge gap in the first cycles, its performance is diminishing after tens of discharge/charge cycles. Figure 3d,e shows the galvanostatic discharge and charge cycling diagrams at the current density of 5 mA cm^{-2}. The discharge voltage of the $Pt/C + RuO_2$ cathode (≈1.26 V) is initially higher but it decreases over cycling to around 1.17 V after 20 cycles and it remains lower than the 1.2 V. The charge potential is not stable and gradually increases when cycled at 5 mA cm^{-2}. Similar behavior is observed for the Con-C (Figure 4d). The poor cycling stability of the $Pt/C + RuO_2$ cathode is frequently observed in rechargeable zinc–air batteries, and it is attributed to the aggregation of the active metal catalysts or degradation of the binder. Moreover, the Nafion binder added to the powdery catalyst slurry could complicate the access of the reactant to the catalyst sites and thus could reduce the performance of the whole device.

Notably, the binder-free SCL-C cathode provides the best cycling performance. The charge–discharge voltage gap is even improved after 150 cycles and continuous 50 h operation at 5 mA cm^{-2}, demonstrating the superior stability and resilience of the SCL-C as a crucial performance factor. The round-trip efficiency is about 63% after 150 cycles. The Con-C performance is significantly lower than the SCL-C in terms of the charge/discharge voltages and cycling stability.

To further elucidate the impact of the oxidation process, the zinc–air battery performance was evaluated for SCL-C cathodes with different oxygen contents. **Figure 5**a shows the discharge profiles for chemically treated GDLs with different oxidation times, GDL (0 h), SCL-C1 (1 h), SCL-C5 (5 h), SCL-C (10 h). The discharge potential is apparently improved upon longer oxidation time. At 10 mA cm^{-2}, the discharge potential is increased from 0.86 V to higher than 1.2 V on carbon paper after oxidation treatment for a few hours. The contact-angle measurement verifies that the surface wettability gradually increases for longer treatment times. Electrochemical impedance was evaluated at

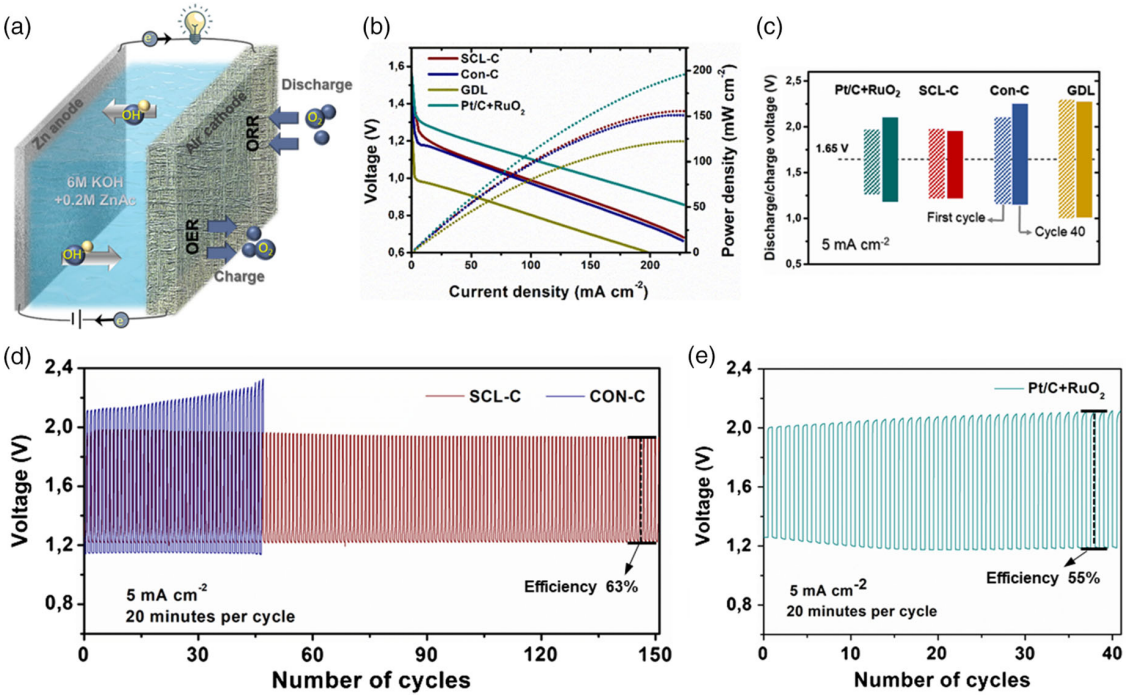

Figure 4. a) Schematic illustration of a rechargeable zinc–air battery, b) galvanodynamic discharge polarization and power density curves of the different electrodes, c) charge and discharge voltages of the electrodes at the first and 40th cycles, d) galvanostatic charge–discharge cycling test of the SCL-C and Con-C electrodes, and e) galvanostatic charge–discharge cycling test of the Pt/C + RuO_2 electrode. The charge and discharge times are 10 min for the cycling tests.

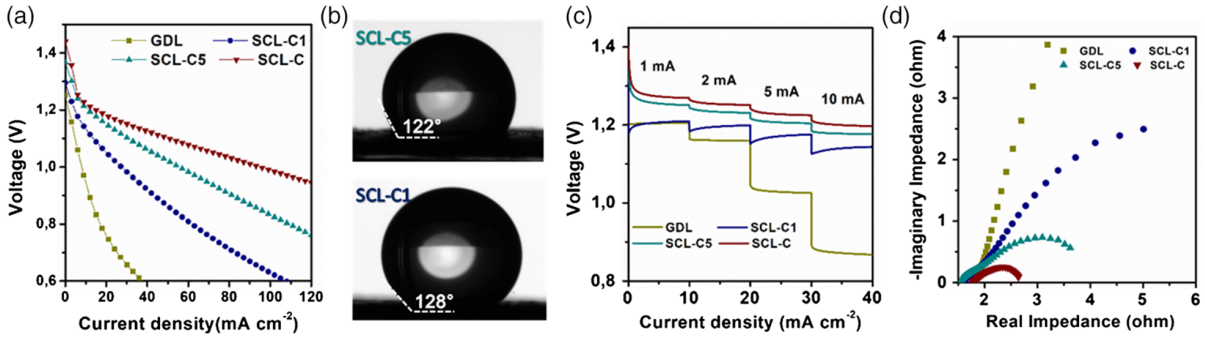

Figure 5. Collected results for the cathodes with SCL and several different treatment times. a) Galvanodynamic discharge polarization curves, b) contact angles of the cathodes with two different treatment times, c) discharge curves at current densities 1 to 10 mA cm^{-2}, and d) impedance curves at 1.1 V.

1.1 V versus Zn/Zn+. The Nyquist plots reveal that the ohmic resistance is slightly reduced on oxidized samples and it has the lowest value (≈1.5 ohm) on the SCL-C5 carbon paper. However, the charge-transfer resistance encountered during the ORR is significantly reduced for longer oxidation time with the lowest value on the SCL-C. This resistance includes the charge transfer during the reaction and the transport of the reactant to the electrode surface.

The overall results demonstrate that the SCL-C can serve as a robust and sustainable electrode with the capability of providing a low charge–discharge gap in a zinc–air battery. The efficiency and stability can be still improved with integrating an auxiliary OER layer to the cathode (Figure 1c). In a proof-of-concept device, the OER- permeable layer is fabricated from nickel foam with a 3D mesoporous surface fully covered with free-standing nanosheets of catalytic NiFe-layered double hydroxide (LDH) directly grown on the foam (see inset in the **Figure 6**a). NiFe-LDH was chosen due to its outstanding OER activity superior to other OER catalysts in basic electrolytes.[39,40] Various alternative catalysts of nonprecious metal-based materials with appealing catalytic activity are studied for OER including metal oxides, metal hydroxides, chalcogenides, and perovskites. Among them, NiFe-LDH is the most attractive material with an outstanding OER activity.[39–42] However, the low electronic

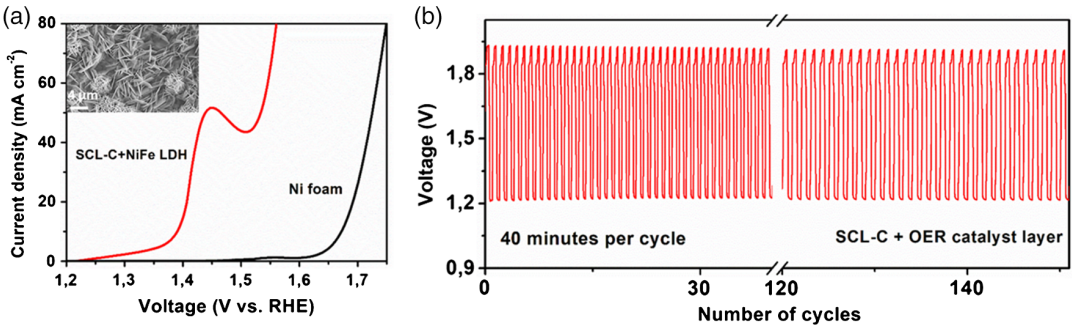

Figure 6. a) Polarization curves within the OER potential window for NiFe-LDH and Ni foam, and an SEM image of the nanosheets is shown in the inset; b) galvanostatic charge–discharge cycling test of the SCL cathode with the auxiliary NiFe-LDH catalyst layer (Figure 1c).

conductivity substantially restricts the performance of the metal oxide catalysts. Direct growth of the catalyst on a porous 3D current collector is an effective approach to circumvent the issue of the low electric conductivity and to create enormous active surface area with low transport resistance of the reactants. The chemical composition of the NiFe-LHD nanostructures was characterized by XPS (Figure S9, Supporting Information). The survey spectrum indicates the presence of the Ni, Fe, O, C, and F elements. The element composition identified by XPS indicates the Fe to Ni ratio of 0.46 in NiFe-LDH nanosheets. The oxygen peak shown in the XPS spectrum originates from the hydroxyl groups in LDH and the absorbed water on the surface of the NiFe-LDH nanosheets. The high-resolution Fe $2p_{3/2}$ and Ni $2p_{3/2}$ peaks are shown in Figure S9, Supporting Information, as well. The Fe $2p_{3/2}$ peak is deconvoluted to several peaks assigned to the Fe^{+3} and Fe^{+2}, where the dominant peak at 713 eV is from the Fe^{+3} coordinated to the OH group.[43,44]

The OER performance of the NiFe-LDH was evaluated in a three-electrode electrochemical set-up in 1 M KOH. The iR-corrected LSV curve shown in Figure 6a indicates impressive OER activity of the NiFe-LDH, which is apparently superior to the RuO_2 catalysts. The cathode with the SCL and the hydrophobic NiFe catalyst layer is tested in a practical two-electrode battery, in which the NiFe-LDH performs as OER catalyst and the SCL as the ORR/OER active region. Figure S10, Supporting Information, displays the optical image of the typical electrodes used for the measurements. The electrolyte flows freely through the nickel foam that is firmly attached to the GDL electrode. The cell charge voltage is lower in the cathode comprising the NiFe-LDH layer than the SCL-C. Figure 6b shows a charge/discharge cycle test of the cell at 5 mA cm^{-2}.

It is notable that the charge/discharge voltage gap of the SCL cathode is only slightly reduced after adding the NiFe-LDH layer, which implies significant OER activity of the SCL-C. To further elucidate that, we compare our results with previous reports on

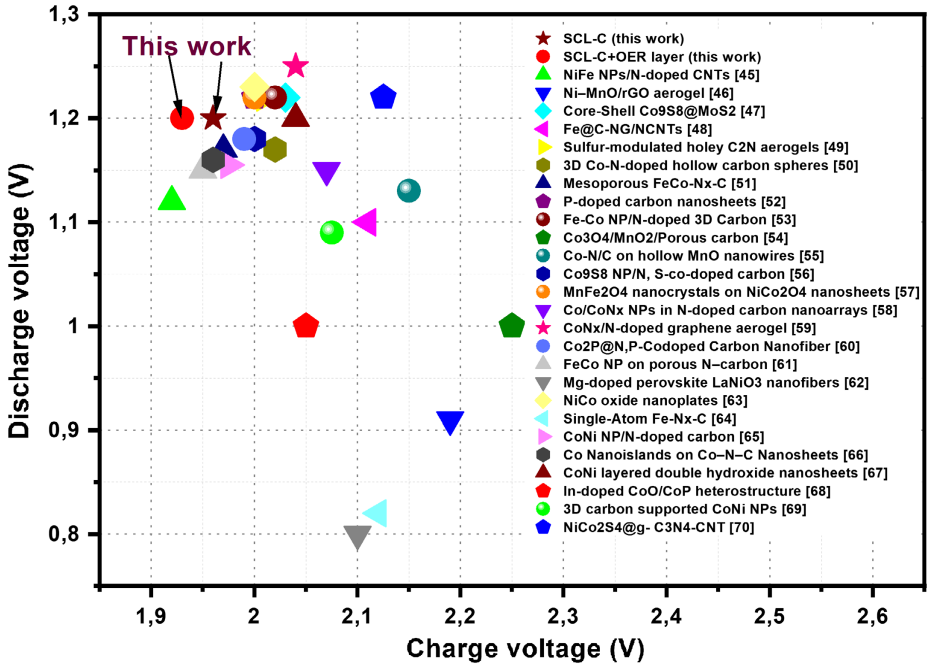

Figure 7. Charge/discharge voltages of the zinc–air batteries with various catalysts cycled at 10 mA cm^{-2}, collected from the most cited articles recently (since 2018) published in literature.[45–70]

best-performing cathodes in zinc–air batteries. **Figure 7** shows the charge/discharge voltages of the rechargeable zinc–air batteries with various air-cathode catalysts, collected from the works recently published in the literature. It is notable that the battery performance with the SCL air-cathode is superior to the majority of best-performing cells comprising carbon-based or metal-containing catalysts. The battery with the SCL-C is among the few cells that surpass the round-trip efficiency of 60% at the current density of 10 mA cm^{-2}. Adding the auxiliary OER active layer reduces further the charge voltage and could enhance the durability of the cathode.

A novel paradigm for design of bifunctional air-cathodes of metal–air batteries is proposed to address the issues with the intricate multiphase catalysts interface involved in the conventional air-cathode assemblies. Incorporating catalytic centers into the cathode bulk increases the number of catalytic active centers with an optimized and stable multiphase interface, and facilitates the mass transfer of the reactants on a mechanically stable structure with a high electric conductivity. Therefore, the battery performance is significantly improved using this modified cathode in terms of the power density, charge/discharge potential and stability, in comparison to the conventional loading of various catalysts on the GDL.

Experimental Section

Chemical Surface Oxidation of the Carbon Materials: The chemical surface oxidation of carbon materials was carried out using nitric acid (70%). For the GDL carbon paper (Sigracet 38 BC, SGL carbon), typically a piece (3.0 cm × 1.2 cm) of the paper was transferred into a sealed glass container with 40 mL acid and heated at 100 °C in an oven for different time spans. Subsequently, the carbon paper was washed with a copious amount of distilled water and dried at 60 °C for 24 h. For the carbon black, 30 mg acetylene carbon black and 50 mL nitric acid were transferred to a sealed glass container equipped with a magnetic stirrer. The solution was heated at the temperature of 100 °C for 10 h. The prepared slurry was centrifuged several times until the neutral pH. Subsequently, the collected powder was dried at 60 °C for 24 h.

Plasma Treatment of the Carbon Paper: Carbon paper samples were treated in a radiofrequency (13.56 MHz) capacitively coupled plasma system at the applied power of 200 W. Two different gas compositions were used; 1) argon flow 30 sccm, and 2) argon (29 sccm) and oxygen (1 sccm) mixture. The operating pressure was 20 Pascal. The treatment time for samples presented here was 3 min.

Synthesis of NiFe LDH Nanosheets: A mixture of 1 mmol of Iron (III) nitrate nonahydrate, 1 mmol of Nickel(II) nitrate hexahydrate (99.999%), and 200 mg of urea was dissolved in 15 mL of deionized water under stirring for 20 min to form a uniform and transparent solution. The nickel foam cut into smaller size of 3.0 cm × 2.0 cm was cleaned with solvents. The foam and the solution were transferred into a Teflon-lined stainless-steel autoclave. The hydrothermal reaction was carried out at 120 °C for 12 h.

Material Characterization: The surface morphology was analyzed by a SEM from Zeiss (Ultra 55 Plus). The surface chemical bonds were studied by XPS on an ESCALAB XI^+ instrument, ThermoFisher. The base pressure during spectra acquisition was better than 5×10^{-7} mbar achieved by an Edwards E2M28 rotary vane pump. The main background gases in the analysis chamber was argon at all points during the loading, pumping, and measurements. The excitation source was a monochromated aluminium anode with an excitation energy of 1486.68 eV operated at approximately 15 kV and 15 mA, giving a source power of 225 W. The work function of the spectrometer was determined by the software as 4.68 eV. The calibration and linearity of the binding energy scale was confirmed with three reference standards which were sputter-cleaned with the ion gun prior to measurement, Au $4f_{7/2}$ (83.96 eV), Ag $3d_{5/2}$ (368.21 eV), and Cu $2p_{3/2}$ (932.62 eV). The latest linearity calibration (measured every 6 months) returned values of 83.92 eV for the Au $4f_{7/2}$ peak, 368.22 eV for the Ag $3d_{5/2}$ peak, and 932.59 eV for the Cu $2p_{3/2}$ peak. With the selected scan parameters, the energy resolution was 0.1 eV for high-resolution spectra and 1 eV for survey spectra. The size of the analyzed sample area was 650 µm and takes the form of an elongated circle. Charge compensation, by means of an electron beam, was applied via a flood gun operated at 100 µA. The charge referencing method was performed by shifting the asymmetric Pt $4f_{7/2}$ peak of freshly sputter-cleaned Pt foil to 71.2 eV.

Electrochemical Measurements: All the electrochemical measurements were carried out on an electrochemical workstation (WaveDriver 200 from Pine) in a standard three-electrode configuration at room temperature. The reference electrode was Ag/AgCl (3 M KCl) and a Pt coil served as the counter electrode. The electrodes were stabilized by cycling for 20 times CV scans at a scan rate 20 mV s^{-1}. All the LSVs were measured at a scan rate of 5 mV s^{-1} and the OER/ORR LSV curves were corrected for the iR compensation. For the OER, the carbon paper samples were directly tested as the working electrode with the immersed area of 1 cm × 1 cm. Furthermore, the powdery carbon black or the precious metal catalysts were prepared by dispersing 5 mg of the powder, and 50 µL of 5 wt% Nafion solution in 1 mL of deionized water and sonication for 30 min. The control precious catalyst powder consisted of 2.5 mg Pt/C (20 wt% on Vulcan XC72) and 2.5 mg RuO_2 (99.9%, Sigma Aldrich), which were mechanically mixed together. Unless otherwise stated, the catalyst ink loading on the carbon paper was 0.8 mg cm^{-2}. The ORR measurements were carried out with O_2 and N_2 saturated KOH solutions. The LSV curves were collected by a rotating disk electrode technique with the speed rate 1600 rpm. For ORR measurements, the carbon paper cut into the circular pieces (0.36 cm^{-3}) were adhered to the glassy carbon disk using Nafion. Electrochemical impedance spectroscopy (EIS) was performed over the frequency range of 1 Hz to 100 kHz.

The electrochemical capacitance was evaluated from the CV curves collected in a potential window −50 to 50 mV (vs Ag/AgCl) where the faradic current was negligible. Half value of the capacitive current ($J_{anodic} - J_{cathodic}$) measured at 0.0 V was plotted against the scan rate (Figure 2b), and the double layer capacitance was estimated from the slope of the linear fit of the data.

The zinc–air batteries were tested in a home-built electrochemical cell in a two-electrode configuration. The carbon paper and the NiFe-LDH/Ni foam samples with the exposed area 1 cm^2 were directly used to serve as the self-standing air-cathode. For the powdery samples, the catalyst ink was loaded on the pristine carbon paper. The electrolyte was 6 M KOH containing 0.2 M zinc acetate, and a Zn plate with thickness 0.8 mm was used as the anode. The gap between the two electrodes was 5 mm.

Supporting Information

Supporting Information is available from the Wiley Online Library or from the author.

Acknowledgements

This work was partially supported by EPSRC (EP/R008841/1).
Open access funding enabled and organized by Projekt DEAL.

Conflict of Interest

The authors declare no conflict of interest.

Data Availability Statement

Data available on request from the authors.

Keywords

air-cathodes, electrocatalyst interfaces, oxygen evolution reaction catalysts, oxygen reduction reaction catalysts, zinc–air batteries

Received: November 16, 2020
Revised: January 8, 2021
Published online: March 9, 2021

[1] J. Pan, Y. Y. Xu, H. Yang, Z. Dong, H. Liu, B. Y. Xia, *Adv. Sci.* **2018**, *5*, 1700691.
[2] C. Han, W. Li, H.-K. Liu, S. Dou, J. Wang, *Mater. Horiz.* **2019**, *6*, 1812.
[3] J. Fu, Z. P. Cano, M. G. Park, A. Yu, M. Fowler, Z. Chen, *Adv. Mater.* **2017**, *29*, 1604685.
[4] Y. Huang, Y. Wang, C. Tang, J. Wang, Q. Zhang, Y. Wang, J. Zhang, *Adv. Mater.* **2019**, *31*, 1803800.
[5] J. Zhang, G. Chen, K. Müllen, X. Feng, *Adv. Mater.* **2018**, *30*, 1800528.
[6] R. Paul, F. Du, L. Dai, Y. Ding, Z. L. Wang, F. Wei, A. Roy, *Adv. Mater.* **2019**, *31*, 1805598.
[7] S. Ren, X. Duan, S. Liang, M. Zhang, H. Zheng, *J. Mater. Chem. A* **2020**, *8*, 6144.
[8] D. Yang, L. Zhang, X. Yan, X. Yao, *Small Methods* **2017**, *1*, 1700209.
[9] J. Pan, X. L. Tian, S. Zaman, Z. Dong, H. Liu, H. S. Park, B. Y. Xia, *Batter. Supercaps* **2019**, *2*, 336.
[10] J. Fu, R. Liang, G. Liu, A. Yu, Z. Bai, L. Yang, Z. Chen, *Adv. Mater.* **2019**, *31*, 1805230.
[11] K. B. Ibrahim, M.-C. Tsai, S. A. Chala, M. K. Berihun, A. W. Kahsay, T. A. Berhe, W.-N. Su, B.-J. Hwang, *J. Chin. Chem. Soc.* **2019**, *66*, 829.
[12] Y. Li, H. Dai, *Chem. Soc. Rev.* **2014**, *43*, 5257.
[13] X.-T. Wang, T. Ouyang, L. Wang, J.-H. Zhong, T. Ma, Z.-Q. Liu, *Angew. Chem., Int. Ed.* **2019**, *131*, 13425.
[14] L.-N. Lu, C. Chen, K. Xiao, T. Ouyang, J. Zhang, Z.-Q. Liu, *Catal. Sci. Technol.* **2020**, *10*, 7256.
[15] H. Su, X.-T. Wang, J.-X. Hu, T. Ouyang, K. Xiao, Z.-Q. Liu, *J. Mater. Chem. A* **2019**, *7*(39), 22307.
[16] H. Cheng, M.-L. Li, C.-Y. Su, N. Li, Z.-Q. Liu, *Adv. Funct. Mater.* **2017**, *27*, 1701833.
[17] C.-Y. Su, H. Cheng, W. Li, Z.-Q. Liu, N. Li, Z. Hou, F.-Q. Bai, H.-X. Zhang, T.-Y. Ma, *Adv. Energy Mater.* **2017**, *7*, 1602420.
[18] Z.-Q. Liu, H. Cheng, N. Li, T. Y. Ma, Y.-Z. Su, *Adv. Mater.* **2016**, *28*, 3777.
[19] Y. Chen, I. Kone, Y. Gong, A. Xie, H. Hu, D. Kong, J. Liu, Y. Tang, X. Yang, R. Pang, *Carbon* **2019**, *152*, 325.
[20] M. Busch, N. B. Halck, U. I. Kramm, S. Siahrostami, P. Krtil, J. Rossmeisl, *Nano Energy* **2016**, *29*, 126.
[21] Z.-F. Huang, J. Song, S. Dou, X. Li, J. Wang, X. Wang, *Matter* **2019**, *1*, 1494.
[22] T. Zhou, N. Zhang, C. Wu, Y. Xie, *Energy Environ. Sci.* **2020**, *13*, 1132.
[23] Y. Wang, Y. Zou, L. Tao, Y. Wang, G. Huang, S. Du, S. Wang, *Nano Res.* **2019**, *12*, 2055.
[24] C. Tang, H.-F. Wang, Q. Zhang, *Acc. Chem. Res.* **2018**, *51*, 881.
[25] M. Qiao, C. Tang, L. C. Tanase, C. M. Teodorescu, C. Chen, Q. Zhang, M.-M. Titirici, *Mater. Horiz.* **2017**, *4*, 895.
[26] J. Snyder, T. Fujita, M. W. Chen, J. Erlebacher, *Nat. Mater.* **2010**, *9*, 904.
[27] Y. Li, H. Zhang, T. Xu, Z. Lu, X. Wu, P. Wan, X. Sun, L. Jiang, *Adv. Funct. Mater.* **2015**, *25*, 1737.
[28] Z. Lu, W. Zhu, X. Yu, H. Zhang, Y. Li, X. Sun, X. Wang, H. Wang, J. Wang, J. Luo, *Adv. Mater.* **2014**, *26*, 2683.
[29] Z. R. Yue, W. Jiang, L. Wang, S. D. Gardner, C. U. Pittman Jr, *Carbon* **1999**, *37*, 1785.
[30] J. L. Figueiredo, M. F. R. Pereira, M. M. A. Freitas, J. J. M. Orfao, *carbon* **1999**, *37*, 1379.
[31] K. Tammeveski, K. Kontturi, R. J. Nichols, R. J. Potter, D. J. Schiffrin, *J. Electroanal. Chem.* **2001**, *515*, 101.
[32] G. Jürmann, D. J. Schiffrin, K. Tammeveski, *Electrochim. Acta* **2007**, *53*, 390.
[33] Z. Liu, Z. Zhao, Y. Wang, S. Dou, D. Yan, D. Liu, Z. Xia, S. Wang, *Adv. Mater.* **2017**, *29*, 1606207.
[34] Z. Lu, G. Chen, S. Siahrostami, Z. Chen, K. Liu, J. Xie, L. Liao, T. Wu, D. Lin, Y. Liu, *Nat. Catal.* **2018**, *1*, 156.
[35] J. Xu, W. Huang, R. L. McCreery, *J. Electroanal. Chem.* **1996**, *410*, 235.
[36] C. Song, J. Zhang, *PEM Fuel Cell Electrocatalysts and Catalyst Layers*, Springer, London **2008**, pp. 89–134.
[37] A. Gabe, R. Ruiz-Rosas, C. González-Gaitán, E. Morallón, D. Cazorla-Amorós, *J. Power Sources* **2019**, *412*, 451.
[38] I. Kruusenberg, J. Leis, M. Arulepp, K. Tammeveski, *J. Solid State Electrochem.* **2010**, *14*, 1269.
[39] J. Mohammed-Ibrahim, *J. Power Sources* **2020**, *448*, 227375.
[40] F. Dionigi, P. Strasser, *Adv. Energy Mater.* **2016**, *6*, 1600621.
[41] C. C. McCrory, S. Jung, J. C. Peters, T. F. Jaramillo, *J. Am. Chem. Soc.* **2013**, *135*, 16977.
[42] Z. W. Seh, J. Kibsgaard, C. F. Dickens, I. B. Chorkendorff, J. K. Nørskov, T. F. Jaramillo, *Science* **2017**, *355*, eaad4998.
[43] A. P. Grosvenor, B. A. Kobe, M. C. Biesinger, N. S. McIntyre, *Surf. Interface Anal. Int. J. Devoted Dev. Appl. Tech. Anal. Surf. Interfaces Thin Films* **2004**, *36*, 1564.
[44] B. P. Payne, M. C. Biesinger, N. S. McIntyre, *J. Electron Spectrosc. Relat. Phenom.* **2009**, *175*, 55.
[45] D. Bin, B. Yang, C. Li, Y. Liu, X. Zhang, Y. Wang, Y. Xia, *ACS Appl. Mater. Interfaces* **2018**, *10*, 26178.
[46] G. Fu, X. Yan, Y. Chen, L. Xu, D. Sun, J.-M. Lee, Y. Tang, *Adv. Mater.* **2018**, *30*, 1704609.
[47] J. Bai, T. Meng, D. Guo, S. Wang, B. Mao, M. Cao, *ACS Appl. Mater. Interfaces* **2018**, *10*, 1678.
[48] Q. Wang, Y. Lei, Z. Chen, N. Wu, Y. Wang, B. Wang, Y. Wang, *J. Mater. Chem. A* **2018**, *6*, 516.
[49] S. S. Shinde, C. H. Lee, J.-Y. Yu, D.-H. Kim, S. U. Lee, J.-H. Lee, *ACS Nano* **2018**, *12*, 596.
[50] S. Chen, J. Cheng, L. Ma, S. Zhou, X. Xu, C. Zhi, W. Zhang, L. Zhi, J. A. Zapien, *Nanoscale* **2018**, *10*, 10412.
[51] S. Li, C. Cheng, X. Zhao, J. Schmidt, A. Thomas, *Angew. Chem. Int. Ed.* **2018**, *57*, 1856.
[52] W. Lei, Y.-P. Deng, G. Li, Z. P. Cano, X. Wang, D. Luo, Y. Liu, D. Wang, Z. Chen, *ACS Catal.* **2018**, *8*, 2464.
[53] X. Liu, L. Wang, P. Yu, C. Tian, F. Sun, J. Ma, W. Li, H. Fu, *Angew. Chem. Int. Ed.* **2018**, *57*, 16166.
[54] X. Li, F. Dong, N. Xu, T. Zhang, K. Li, J. Qiao, *ACS Appl. Mater. Interfaces* **2018**, *10*, 15591.
[55] Y.-N. Chen, Y. Guo, H. Cui, Z. Xie, X. Zhang, J. Wei, Z. Zhou, *J. Mater. Chem. A* **2018**, *6*, 9716.
[56] Y. Li, W. Zhou, J. Dong, Y. Luo, P. An, J. Liu, X. Wu, G. Xu, H. Zhang, J. Zhang, *Nanoscale* **2018**, *10*, 2649.
[57] Y.-Q. Zhang, M. Li, B. Hua, Y. Wang, Y.-F. Sun, J.-L. Luo, *Appl. Catal. B Environ.* **2018**, *236*, 413.
[58] C. Guan, A. Sumboja, W. Zang, Y. Qian, H. Zhang, X. Liu, Z. Liu, D. Zhao, S. J. Pennycook, J. Wang, *Energy Storage Mater.* **2019**, *16*, 243.
[59] H. Zou, G. Li, L. Duan, Z. Kou, J. Wang, *Appl. Catal. B Environ.* **2019**, *259*, 118100.

[60] J. Gao, J. Wang, L. Zhou, X. Cai, D. Zhan, M. Hou, L. Lai, *ACS Appl. Mater. Interfaces* **2019**, *11*, 10364.
[61] J. Liu, T. He, Q. Wang, Z. Zhou, Y. Zhang, H. Wu, Q. Li, J. Zheng, Z. Sun, Y. Lei, *J. Mater. Chem. A* **2019**, *7*, 12451.
[62] J. Bian, R. Su, Y. Yao, J. Wang, J. Zhou, F. Li, Z. L. Wang, C. Sun, *ACS Appl. Energy Mater.* **2019**, *2*, 923.
[63] J. Zhao, Y. He, Z. Chen, X. Zheng, X. Han, D. Rao, C. Zhong, W. Hu, Y. Deng, *ACS Appl. Mater. Interfaces* **2018**, *11*, 4915.
[64] J. Han, X. Meng, L. Lu, J. Bian, Z. Li, C. Sun, *Adv. Funct. Mater.* **2019**, *29*, 1808872.
[65] L. Yang, D. Wang, Y. Lv, D. Cao, *Carbon* **2019**, *144*, 8.
[66] P. Yu, L. Wang, F. Sun, Y. Xie, X. Liu, J. Ma, X. Wang, C. Tian, J. Li, H. Fu, *Adv. Mater.* **2019**, *31*, 1901666.
[67] T. Wang, J. Wu, Y. Liu, X. Cui, P. Ding, J. Deng, C. Zha, E. Coy, Y. Li, *Energy Storage Mater.* **2019**, *16*, 24.
[68] W. Jin, J. Chen, B. Liu, J. Hu, Z. Wu, W. Cai, G. Fu, *Small* **2019**, *15*, 1904210.
[69] W. Wan, X. Liu, H. Li, X. Peng, D. Xi, J. Luo, *Appl. Catal. B Environ.* **2019**, *240*, 193.
[70] X. Han, W. Zhang, X. Ma, C. Zhong, N. Zhao, W. Hu, Y. Deng, *Adv. Mater.* **2019**, *31*, 1808281.